Cryogenic vacuum chamber testing of a conductively-cooled, high temperature superconducting rotor for a 1.4 MW electric machine for aeronautics applications

Justin J. Scheidler[1], Erik J. Stalcup[1], Thomas F. Tallerico[1], William Torres[2], Kirsten P. Duffy[3], Tysen T. Mulder[1]

[1]NASA Glenn Research Center, Cleveland, OH, 44135, USA
[2]Wolf Creek Federal Services, Cleveland, OH, 44135, USA
[3]University of Toledo, Toledo, OH, 43606, USA

Email: justin.j.scheidler@nasa.gov

Abstract. This paper presents the second ever demonstration of a superconducting rotor cooled only via conductive connection to a cryocooler, i.e., without pumped or solid cryogens. The full-scale rotor was operated statically in its intended environment – about 1e-3 torr vacuum with only conductive cooling through mechanical connections to a cryocooler contained on the rotor. Stable operation of the rotor in a representative magnetic environment was demonstrated up to its rated direct current (57.2 A) and the designed temperature limit for the superconductor (62 K). Additional electrical measurements increased confidence that the superconducting coils functioned as intended. A collection of steady state temperature distributions was measured at operating and non-operating conditions. In all but one case, the observed temperature gradient between the cold tip and superconducting coils satisfies the design but with little margin. Opportunities to reduce the gradient are identified.

1. Introduction

Aviation's impact on our climate is caused by greenhouse gas emissions and contrails, with CO_2 emissions having the dominant impact. Over the past 40 years, improvements in gas turbine engines and other technologies have fueled a more than 60% reduction in CO_2 emissions per kilometer flown by each passenger [1]. Despite that significant progress in efficiency, global CO_2 emissions from aviation continue to grow at an increasing rate. Aviation's share of the total, human-caused CO_2 emissions has increased [1] and is expected to continue doing so unless bold actions are taken. The climate and air quality impacts of aviation can be reduced by switching to an energy source that has a lower well-to-wake environmental impact (e.g., liquid hydrogen produced using renewable energy) or by reducing the energy required by the aircraft to complete its typical mission(s). Electrified aircraft propulsion (EAP) can enable meaningful reductions in energy use and help enable zero emissions through changes in energy source. However, lighter and more efficient electric motors and generators are required to enable net energy reductions with EAP, especially for the large transport aircraft (about 150+ passengers) that produce most of aviation's emissions [2], [3], [4]. At this scale, electrified propulsion systems with 1 to 30+ MW components are required. Superconducting and cryogenic electric machines are two options that can meet this demand for EAP systems with component ratings around 1 MW and may be the only viable options when component ratings approach or exceed 10 MW.

To achieve a reduction in energy use after adding an EAP system to the aircraft, the performance of the electrified propulsion components must exceed the state of the art. Not only must the specific power of electric machines improve to limit the mass of the system, but their efficiency must also improve to limit waste heat (which necessitates added mass for a thermal management system) and limit oversizing other electrified propulsion components (which must overcome the machines' inefficiency). In numerous cases, the efficiency of electric machines has a stronger influence on an aircraft's energy use than their specific power. Superconducting and cryogenic machines typically can achieve higher efficiency than their counterparts that operate above ambient temperature.

NASA's high efficiency megawatt motor (HEMM) is a partially superconducting, 1.4 MW electric machine designed for electrified aircraft propulsion. It has performance targets of greater than 98% efficiency and 16 kW/kg electromagnetic specific power[1]. HEMM's high performance is achieved through the use of a superconducting rotor composed of twelve 2nd generation high temperature superconducting (HTS) coils that are designed to operate at temperatures below 62 K. The development of HEMM's electromagnetic design was supported by testing sub-scale and full-scale superconducting coils in liquid nitrogen (LN_2), and the authors have previously published this experimental work [5], [6], [7]. Although these LN_2 tests have reduced multiple risks in HEMM's rotor design, they did not test the HTS coils at their designed thermo-electro-magnetic operating condition. This paper presents the first test of HEMM's rotor where the HTS coils were conductively cooled to their rated operating temperature and then excited at their rated operating current and magnetic field. A recent paper by the authors detailed the test setup, the differences between the HEMM design and the test, and the first round of electrical measurements [8]. This paper summarizes those topics and presents a complete set of electrical and thermal measurements, along with a discussion of the data and ways to improve performance.

2. Overview of HEMM and its superconducting rotor

HEMM is designed to produce 2 kNm of torque at a speed of 6,800 rpm. HEMM's stator employs a copper armature winding that is oil cooled and operates at an average temperature around 423 K (150 °C) [9]. The superconducting rotor is conductively cooled to cryogenic temperatures using a rotating cryocooler embedded inside the machine's shaft. The entire cryogenic system is contained within the machine, and the aircraft must supply only electrical power to the machine for the cryogenics. Hence, HEMM is a cryogen-free machine that appears to be the same as a non-superconducting machine from the perspective of the aircraft. Each of the twelve field coils is formed by a no-insulation four-layer stack racetrack coil that nominally contains 600 turns of HTS (i.e., 150 turns per racetrack). Each racetrack was wound with as-received, 4 mm wide coated conductor using a tension of 1.5 kg.

2.1. Thermal design of the superconducting rotor

The thermal design of the HEMM rotor is focused on conductively cooling the superconducting coils. The cooling is provided by the integrated pulse tube cryocooler. The primary requirements for the rotor's thermal design are:

- The cryocooler shall provide 51 W of heat lift at 50 K
- The superconducting coils must operate at 62 K or lower

Therefore, the rotor has been designed to minimize the heat load on the cryocooler while keeping the coils at 62 K or lower with a cryocooler cold tip temperature at 50 K.

The primary sources of heat onto the superconducting end of the rotor are conduction from the hot end of the rotor shaft, convective heating and windage losses, radiative heating from the stator, current lead conduction, and resistive heating in the current leads, jumpers between coils, and solder joints. The rotor shaft, shown in Figure 1, is coupled with the heat exchanger at the hot end of the cryocooler which could operate at a temperature around 400 K. To minimize heat conduction along its length, the shaft tapers down to a 1 mm thickness. The shaft is made of Ti-6Al-4V titanium alloy for low thermal

[1] Electromagnetic specific power is defined as the machine's continuous output power divided by the mass of active components inside the machine. A thermal management system is not included in the mass.

conductivity, high specific stiffness, and high specific strength. Additionally, the mechanical interface between the shaft and the rotor backiron has minimal points of contact to further reduce heat transfer. On the backiron side of this interface, a webbed structure extends from the shaft to the bulk of the backiron. The webbed portion of the backiron also reduces heat transfer from the shaft by minimizing the cross-sectional area of the conductive path.

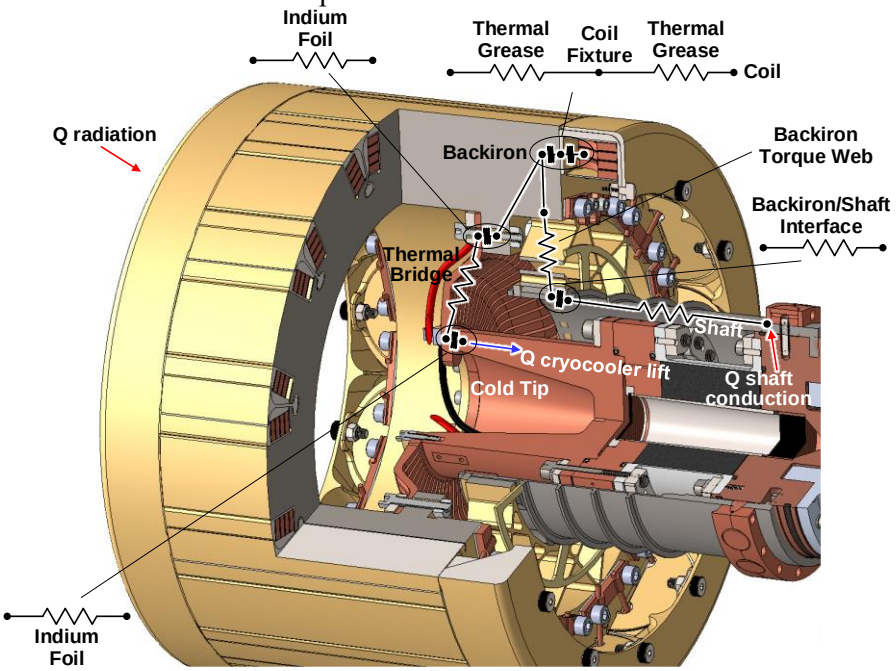

Figure 1. HEMM's superconducting rotor overlaid with simplified thermal resistance network.

Convection and windage losses are another heat source. Heat transfers from the warm stator to the rotor through the air gap in a cylindrical Couette flow. Windage losses are due to frictional heating with the air during rotation [10]. These are mitigated by operating the rotor in a $< 10^{-3}$ torr vacuum enclosure, which was estimated to reduce windage losses to less than 1 W. Radiative heating from the stator can account for another large source of heat. This is mitigated by minimizing the infrared emissivity of rotor and stator surfaces. Fabricated rotor components not composed of smooth copper are coated with gold in a physical vapor deposition (PVD) process that results in a total hemispherical infrared emissivity of 0.018 or lower. The stator must use a non-electrically conductive optical coating to eliminate eddy current losses. A vacuum-compatible low-emissivity paint was selected with an emissivity around 0.13. Patterned metallic coatings were considered but the heat generation due to eddy currents offset the benefit of a lower emissivity.

Heat also enters the rotor via conduction along the direct current leads. Similar to the shaft, the two current leads pick up heat from the hot end of the cryocooler due to their proximity. The leads also generate heat while operating due to resistive Joule heating. These heat sources are mitigated by optimizing the current lead length to minimize the sum of both effects. To allow for the optimum length, the current leads are supported by several insulating brackets before interfacing with the cold tip. The leads are coupled to the cold tip via a thermally conductive but electrically isolated clamping plate to reject the heat away from the coils and minimize heat transfer at the coil terminals. Resistive heating in the coil-to-coil leads is mitigated in a similar way by thermally coupling them to the backiron.

The conductive thermal path from the cold tip to the coils has been designed to maximize heat transfer. One key component is the thermal bridge, which mechanically connects the cryocooler's cold tip to the backiron but minimizes torque transfer. As a result of trades of strength and thermal properties, the thermal bridge is made of a dispersion strengthened copper containing 0.15% aluminum by weight as alumina. The mechanical interfaces between the thermal bridge, cold tip, and backiron have a high thermal contact conductance due to a large bolt pressure, flat polished surfaces, and a 0.058 mm thick

indium foil thermal interface material. The other important interfaces are between the backiron and coils. Based on previous thermal modeling, the primary conduction path from the coils is to the rotor poles through the inner wall of the coil fixtures. The thermal contact conductance at these interfaces is improved by the PVD gold coating and a high-conductance cryogenic vacuum grease. A simplified thermal resistance network of the HEMM rotor is shown in Figure 1.

3. Experimental setup

This section is a summary of the physical assembly of the experiment and its differences from HEMM. For a more detailed discussion, the reader is referred to [8].

A static test of the full-scale HEMM superconducting rotor was conducted in a thermal vacuum chamber at the NASA Glenn Research Center's ICE-Box facility. The experimental setup is depicted in Figure 2. The pressure inside the ICE-Box's pressure vessel was between 7e-4 torr and 1.8e-3 torr at operating temperature during testing. To reduce the cost of the test, only three of HEMM's twelve superconducting rotor coils were manufactured and tested. Even though only three coils were used, the test article was designed such that the non-superconducting current path on the rotor approximately matched the HEMM design. Current was forced to travel the full circumference of the test article's rotor in a representative conductive path by including all the copper coil-to-coil terminals from the HEMM rotor and connecting them in series with copper leads where superconducting coils were missing.

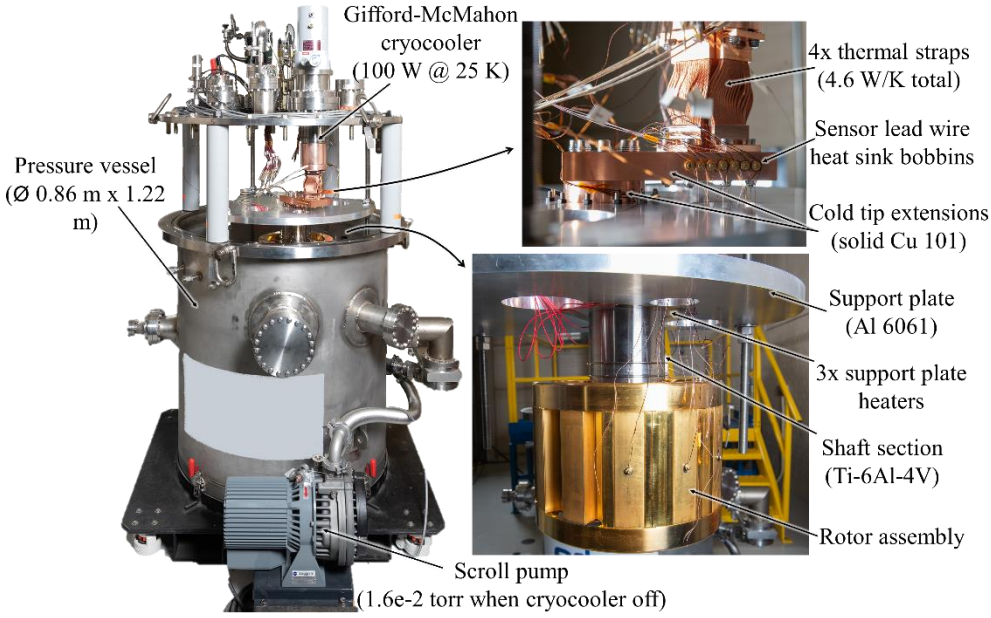

Figure 2. Overall experimental setup.

The full-scale rotor was mechanically supported by a short section of the shaft from the complete machine. The rotor was secured to the shaft using a custom disk spring and snap ring assembly. The shaft was bolted to a large support plate that hung from the lid of the ICE-Box. The plate was heated to maintain a constant temperature ranging from about 0 °C (heaters off) to 90 °C (slightly less than the predicted temperature of the shaft where HEMM's vacuum seal and cryocooler dissipate heat). The length of the shaft section matched the distance between the rotor and these heat sources in the full HEMM design.

Copper thermal straps and two copper cold tip extension blocks were used to connect the test article to the ICE-Box's cryocooler. The thermal connections between the ICE-Box's cryocooler and the location where HEMM's cryocooler would reside in the full machine (the "cold tip") performed well enough to reach a cold tip temperature of 26.3 K, about 5 K colder than what HEMM's cryocooler is expected to reach under no load.

The rotor was instrumented with 16 resistance temperature detectors (RTDs) and 10 Type E thermocouples. Many of these were paired, with one sensor placed on each side of key thermal interfaces. RTDs were used in areas where the magnetic field strength was expected to be higher and higher accuracy was desired. Sensors were mounted using screws where possible. The remaining sensors were attached using varnish and overtaped with an aluminum tape in most locations to provide a closer match to the emissivity of the rotor surfaces. Sensor leads were thermally anchored to the cryocooler cold tip extension by wrapping and varnishing around bobbins. During assembly and testing, five of these sensors were damaged or exhibited anomalous behavior and are not included in the results presented in this paper. The current supplied to the rotor was measured at the power supply. Voltage was measured across the inlet and outlet copper terminals on the back iron and across the copper wires soldered to each superconducting coil.

4. Results and discussion

This section presents the electrical and thermal measurements and discusses them in the context of the health and functionality of the superconducting coils as well as the predicted thermal environment needed to achieve that functionality.

4.1. Electrical results

The results of a first round of electrical characterization were reported in [8]. Those measurements were obtained from the same test configuration as test point A in Section 4.2. In the first round of testing, only the voltage across the rotor's entire circuit was measured. Two steady state voltage versus current responses were measured at a peak coil temperature of about 60.5 K to 61.0 K – one to 45 A and the other to 57.2 A. The steady-state voltage at a current of 57.2 A was also measured as temperature increased from 60.8 K to 62.0 K. During the first measurement, a jump in voltage from about 12 mV to 19 mV occurred while waiting for the voltage to stabilize at a current of 50 A. This observation combined with an increase in the rotor circuit's resistance from 0.22 mΩ in the first measurement to 0.36 mΩ in the second measurement suggested that damage to the superconductor may have occurred. However, stable operation of the rotor at HEMM's design limit for current (57.2 A) and superconductor temperature (62.0 K) was still achieved during the first round of testing after the unexpected behavior.

This paper presents the results of a second round of electrical characterization conducted on the same test configuration as test point F in Section 4.2. Figure 3 depicts the measured voltage across the rotor's current lead terminals and across each superconducting coil. During this measurement, the ICE-Box was operated to maintain a peak temperature in the coils of about 61.0 K. Each voltage is highly linear showing no signs of a transition to the normal state. The rotor exhibited stable operation at 57.5 A. The observed resistance of the right coil (0.008 mΩ) is an order of magnitude smaller than that of the left and central coils (0.086 mΩ and 0.100 mΩ, respectively). This variation in resistance cannot be fully explained by differences in the amount of copper contained between each voltage tap. The cause likely includes sizeable variations in solder joint resistance, but the observation may also indicate damage to the superconductor that caused current sharing with the stabilizer without a detectable nonlinear voltage.

Throughout the test campaign, the rotor assembly sustained a total of 6 thermal cycles between 293 K and < 50 K. A linear voltage response with stable operation up to ≥ 45 A was achieved in 6 separate tests throughout the electrical characterization and thermal testing.

Due to the lack of magnetic sensors, additional electrical measurements were taken to increase confidence that the applied current was properly circulating in the coils. Attempts to directly measure the inductance of the rotor circuit or coils were unsuccessful because low resistance paths existed between the coils and backiron through the coil fixtures. The rotor's inductance was indirectly estimated from measurements of the voltage decay following a change in current. Figure 4 shows the decay that occurred after reaching each current setpoint during the electrical characterization in Figure 3. An exponential function was fit to each curve. The average decay time constant is 609 s with a standard deviation of 70 s. Assuming that the circuit can be represented by a series-connected inductor and resistor, an estimated inductance of 0.15 H is calculated from the time constant and the measured

resistance from the characterization (0.253 mΩ). The voltage decay after a 10 A quasi-step reduction in current was measured at different coil temperatures. The resulting time constants, measured resistances, and estimated inductances at each temperature are tabulated in Table 1. The inductance is again large at a valid operating temperature, but it became too small to quantify with the chosen data acquisition system after the coil temperatures exceeded the critical temperature of the HTS. The credibility of the estimated inductance (L) was assessed by comparing it to a prediction based on 3D finite element results and the equation $L = \frac{1}{I^2}\iiint_V \boldsymbol{J} \cdot \boldsymbol{A}\, dV$ [11], where I is the current, V is the volume of the coils, $\boldsymbol{J}$ is the current density vector, and $\boldsymbol{A}$ is the magnetic vector potential. The experimentally estimated inductance is similar to the predicted inductance (0.52 H), which gives some confidence that the current circulated in the coils as desired but also motivates a more direct measurement of the inductance in the future.

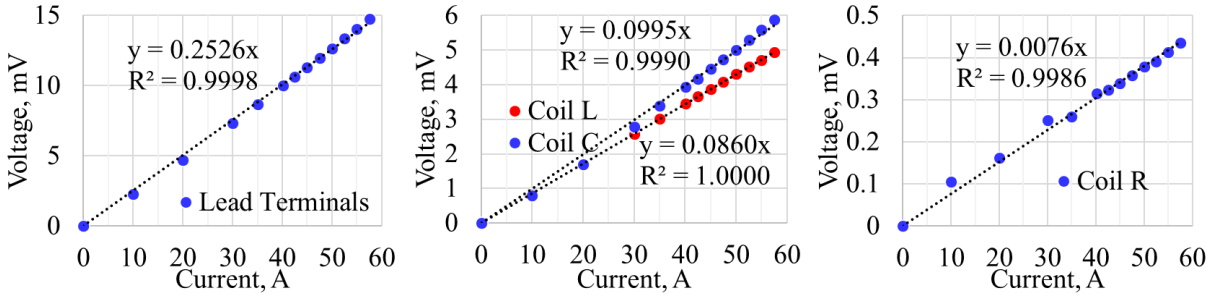

Figure 3. Electrical characterization of the superconducting rotor.

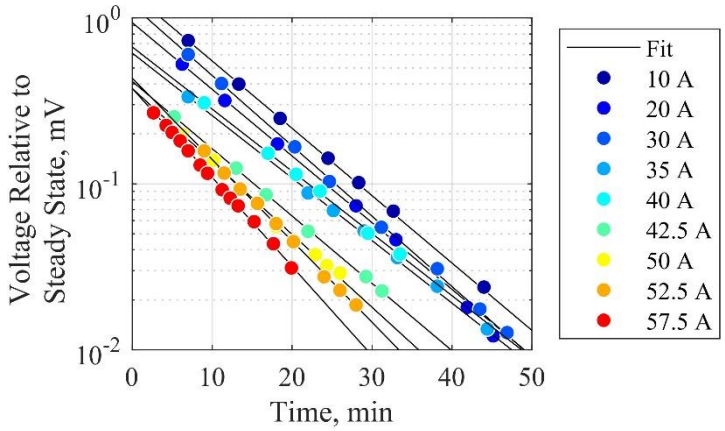

Figure 4. Decay of voltage across the rotor's current leads after reaching different current setpoints during the electrical characterization.

Table 1. Estimated inductance of the rotor circuit at different coil temperatures.

Coil Temperatures, K	Time Constant, s	Rotor Circuit Resistance, mΩ	Inductance, mH
55.8 to 57.4	628	0.253	159
104.3 to 105.6	< 0.2	0.680	< 0.1
300	< 0.2	0.557	< 0.1

4.2. Steady-state thermal results

Temperature data was collected at the test points summarized in Table 2. The data was collected in a stable thermal condition where greater than 90% of the temperature sensors were changing at a rate less than 0.2 K/hr. Electrical data collected at higher rotor currents and discussed in the previous section was collected in a less stable thermal condition. Test points A and B correspond to the first round of electrical testing. Changes to the test configuration took place after test points A and B to improve the thermal performance. All other test points (C-F) were obtained with these changes in place. After test point A, multiple sensor leads were better routed to eliminate or greatly reduce contact with the rotor assembly,

but the heat sinking of one current lead terminal was degraded because a nylon screw head was sheared off during re-assembly. After test point B, a residue (likely residual solder flux) was cleaned off a few surfaces to improve the thermal conductance between the backiron and the current lead terminals. Also at this time, the nylon screws that clamped these terminals to the rotor were replaced with brass screws. Further, accessible sensors mounted with varnish and the current leads exposed to the free end of the rotor were both overtaped with aluminum tape as mentioned above to reduce their emissivity. After test point B, the thermocouples on each side of the shaft to torque web interface were removed; the sensor on the torque web was reinstalled close to its original location, but the sensor on the shaft could only be reinstalled roughly 20 mm closer to the warm end of the shaft. Test points C, D, E, and F are essentially in the same physical configuration.

Table 2. Thermal test points and coil temperatures.

Test Point	Rotor Current (A)	Support Plate Heater Enabled?	HEMM's Cold Tip Temp. (K)	Coil Temp. (K)		ΔT, Cold Tip to Coils (K)	
				Average	Peak	Average	Peak
A	0	Yes	48.2	59.6	60.2	11.3	12.0
B	0	No	26.3	39.1	40.1	12.9	13.8
C	0	No	45.0	55.9	56.6	10.9	11.6
D	0	No	45.0	55.2	55.9	10.2	10.9
E	47.5	No	45.0	55.8	56.7	10.8	11.7
F	0	Yes	45.0	56.6	57.3	11.6	12.3

The cold tip and coil temperature results are also shown in Table 2. The cold tip temperature was measured near the thermal bridge interface and coil temperatures were measured on the coil terminals soldered to the superconducting coils. The cold tip was maintained below 50 K in each test point to provide margin to HEMM's maximum allowable coil temperature of 62 K. At each test point, the coils were maintained below 62 K with temperatures ranging from 37.4 K to 60.2 K. In the full HEMM motor, the cold tip would be at 50 K resulting in an allowable temperature difference (ΔT) of 12 K from the cold tip to the coils. The ability to achieve this condition will be verified using the thermal model after correlation with this test data. In the experiment, with cold tip temperatures below nominal, the observed peak ΔT ranged from 12.0 K to 13.8 K before the improvements were implemented and 10.9 K to 12.3 K after. The improved ΔTs are acceptable but larger than desired and larger than predicted by the uncorrelated model of the HEMM rotor. The results of this experiment will be used to correlate the thermal model and implement design improvements to add thermal margin to the rotor design.

Rotor temperatures during test point E are shown in Figure 5. The ΔTs across interfaces and through components are summarized in Table 3 along with uncorrelated model predictions for point E. The ΔT across the cold tip to thermal bridge interface was small as expected – only 0.4 K on average. Although not directly measured, the ΔT through the thermal bridge was considerably larger than expected. However, this larger ΔT may result from higher-than-expected heat load and not a flaw in the thermal bridge design. Higher-than-expected shaft temperatures near the backiron (217 K average for points C – F) and high backiron torque web temperatures (124 K for point B) suggest that heat leak into the rotor was larger than expected. Additionally, the current lead terminals operated relatively hot with a ΔT to the underlying axial face of the backiron of 33.6 K to 45.5 K before improvements were implemented and an average of 11.8 K after. The reduction in ΔT demonstrates the strong influences of cleanliness and clamping force on the terminal temperatures. The improved ΔT of 11.8 K was however still considerably larger than predicted, suggesting that the heat sinking of the current leads to the cold tip may have underperformed or that there was higher than expected resistive losses in the leads and terminals. Temperature variation throughout the bulk of the backiron was only 1.5 K on average. The ΔT from the terminal soldered onto each coil (expected to be the hottest location in the coils) through the titanium coil fixture and to the backiron pole was less than 1.9 K, only slightly higher than predicted. The measured ΔT between cold tip and coils was likely driven by increased heat loads from heat leak

Table 3. Notable temperature differences at each test point (location 1 minus location 2).

Location 1	Location 2	Test Point A	B	C	D	E	F	Uncorrelated model [8] (point E)
Cold tip at cold tip/ bridge interface	ICE-Box cryocooler cold tip	12.77	8.77	10.79	10.12	11.01	11.72	–
Thermal bridge at cold tip/bridge interface	Cold tip at cold tip/ bridge interface	0.43	0.36	0.41	0.38	0.41	0.45	0.06
Thermal bridge (clamp ring) at bridge/ backiron interface	Thermal bridge at cold tip/ bridge interface	4.54	4.44	4.28	3.93	4.29	4.53	1.45
Large support plate, near heater	Shaft near interface with Al support plate	65.58	-15.85	-14.79	-17.02	-16.04	59.53	-15.81
Shaft near interface with Al support plate	Shaft at shaft/ backiron interface	173.18	151.18	–	–	–	–	–
	Shaft close to shaft/backiron interface	–	–	86.28	78.79	77.71	60.62	185.20
Shaft at shaft/ backiron interface	Backiron at shaft/backiron interface	26.09	22.04	–	–	–	–	–
Backiron at shaft/ backiron interface	Backiron axial face, coil C shaft end	37.60	86.47	–	–	–	–	–
Current lead terminal A	Backiron axial face, coil C shaft end	33.63	45.54	8.56	8.80	9.61	13.33	0.26
Current lead terminal B	Backiron axial face, coil C shaft end	–	–	10.53	12.42	13.31	15.12	0.30
Coil-to-coil terminal, coil L, free end	Backiron axial face, coil C free end	9.52	22.28	4.53	5.06	4.73	4.84	-0.07
Coil terminal coil C, free end	Backiron axial face, coil C free end	1.36	1.11	1.13	1.18	1.22	1.29	0.46
Coil terminal coil C, free end	Backiron pole OD coil C	1.78	1.71	1.74	1.74	1.75	1.87	0.62
Coil terminal coil L, shaft end	Backiron pole OD coil L	0.32	-0.50	-0.16	-0.15	-0.25	0.39	0.46
Coil terminal coil R, free end	Backiron pole OD coil R	1.20	1.17	1.14	1.17	1.08	1.23	0.45
Coil terminal coil C, free end	Cold tip at cold tip/ bridge interface	12.01	13.71	11.60	10.90	11.69	12.30	3.56
Coil terminal coil L, shaft end	Cold tip at cold tip/ bridge interface	10.31	11.12	9.48	8.97	9.39	10.73	3.51
Coil terminal coil R, free end	Cold tip at cold tip/ bridge interface	11.71	13.80	11.62	10.63	11.33	11.90	3.53
Coil terminal coil C, free end	Thermal bridge (clamp ring) at bridge/ backiron interface	7.03	8.91	6.90	6.59	6.99	7.32	2.05
Coil terminal coil L, shaft end	Thermal bridge (clamp ring) at bridge/ backiron interface	5.34	6.32	4.78	4.65	4.69	5.75	2.00
Coil terminal coil R, free end	Thermal bridge (clamp ring) at bridge/ backiron interface	6.73	9.00	6.92	6.32	6.63	6.92	2.02
Current lead terminal A	Coil terminal coil C, free end	31.66	43.10	5.88	6.16	7.15	10.66	-0.23
Current lead terminal B	Coil terminal coil R, free end	–	–	7.82	10.06	11.21	12.84	-0.16

through the shaft and copper lead losses and not a flaw in the cold tip to coil conduction path. Other potential causes of higher heat loads and rotor temperatures may have been higher than expected radiative and/or convective heating.

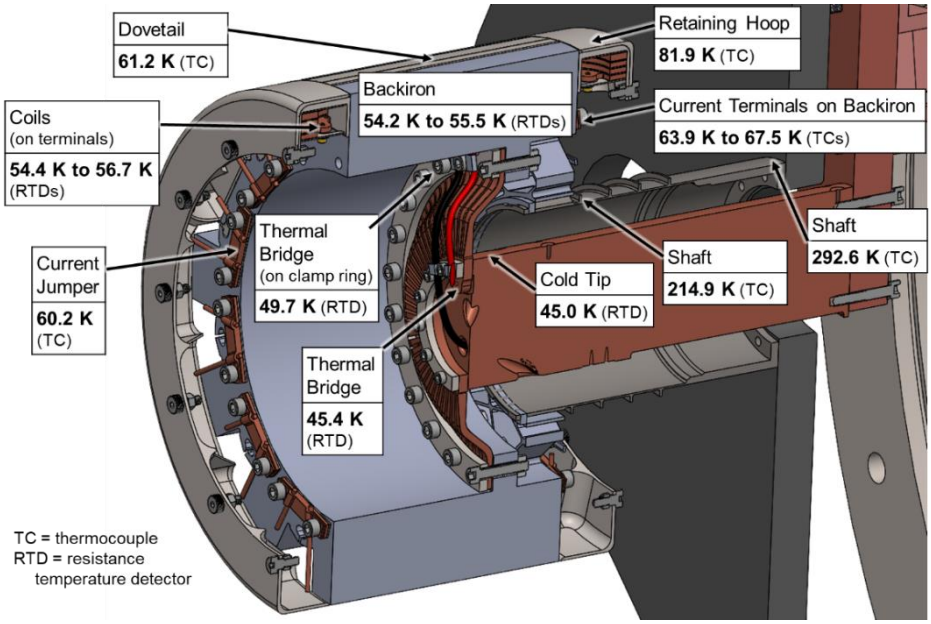

Figure 5. Test point E temperatures (47.5 A operating condition, mount plate heater off).

Heating the support plate by about 80 K only caused the coils and backiron to increase on average by 1.5 K and 1.2 K, respectively. This change in temperatures seems to have primarily resulted from higher conduction through the current leads to the rotor, because the average temperature of the current lead terminals increased by 5.0 K, while the shaft did not appreciably change temperature. The conduction heat load to the rotor through the leads will likely increase in HEMM, because this thermal boundary may reach temperatures 45 K hotter than tested. The large ΔT between the *heated* support plate and shaft (test points A and F) indicates that the thermal conductance between plate and shaft was poor, such that the heated plate increased the radiative loading on the rotor but provided minimal conducted heat. The cause of this poor conductance is likely due to the weight of the rotor assembly and cold tip extensions tending to separate the bolted shaft-to-plate interface, which did not contain a thermal interface material or polished surfaces.

After the improvements, the average ΔT between the dovetail parts and the coils and backiron was 5.9 K and 7.0 K, respectively. This demonstrates there was fairly good thermal coupling between these parts and that the coupling to the coils was better. The retaining hoop and coils were not well thermally coupled as their average ΔT was 25.9 K.

The change in heater power at the ICE-Box cryocooler's cold tip from operational to non-operational (test point E to D) was 7.6 W. Based on the measured resistance of the rotor circuit (0.253 mΩ), the change in Ohmic loss in that circuit was 0.57 W. The uncorrelated thermal model predicts an additional heat load of about 1 W on the cryocooler due to Ohmic loss in the current leads; this prediction is sensitive to the unknown thermal conductance between the current leads and both the cold tip and backiron. Thus, the 6 W discrepancy may reduce after the model is correlated.

5. Conclusions

This paper presented the setup and results of an experiment to demonstrate the full-scale HEMM superconducting rotor in a vacuum chamber up to its rated operating temperature (62 K) and rated current (57.2 A). Throughout the test campaign, the rotor assembly sustained a total of 6 thermal cycles between 293 K and < 50 K. A very linear voltage response with stable operation up to 45 to 57.5 A was achieved in 6 separate tests. The estimated inductance of the rotor was similar to a prediction at operating

temperature and reduced to near zero above the critical temperature of the superconductor. A jump in voltage was observed at 50 A during the first test, but a permanent increase in the rotor's resistance did not result. However, a relatively large variation in the resistance of each of the three superconducting coils was observed, which motivates future disassembly and testing of each coil. At cold tip temperatures 5 K below HEMM's nominal, the observed peak ΔT from the cold tip to the superconducting coils ranged from 10.9 K to 12.3 K after improvements to the setup were implemented. This ΔT is acceptable but provides little to no margin. The temperature measurements and a comparison to an uncorrelated model indicated that the ΔT may be driven by larger than expected heat conduction from the shaft, current leads that were more thermally isolated than anticipated, and/or higher radiative and convective heating. Preliminary ideas to reduce the ΔT include a material change to enable higher clamping force at current lead heat sinks and changes to the shaft's geometry or material processing.

6. References

[1] Lee, D.S. et al., Atmospheric Environment 244, 117834, 2021.
[2] R. H. Jansen, C. Bowman and A. Jankovsky, "Sizing Power Components of an Electrically Driven Tail Cone Thruster and a Range Extender," in 16th AIAA Aviation Technology, Integration, and Operations Conference, Washington, D.C., 2016.
[3] R. H. Jansen, C. Bowman, A. Jankovsky, R. Dyson and J. Felder, "Overview of NASA Electrified Aircraft Propulsion (EAP) Research for Large Subsonic Transports," in 53rd AIAA/SAE/ASEE Joint Propulsion Conference, Atlanta, GA, 2017.
[4] G. V. Brown, "Weights and Efficiencies of Electric Components of a Turboelectric Aircraft Propulsion System," in 49th AIAA Aerospace Sciences Meeting, Orlando, FL, 2011.
[5] J. J. Scheidler, T. F. Tallerico, W. Torres and W. A. Miller, "Risk Reduction Testing of Superconducting Coils for the High Efficiency Megawatt Motor," in AIAA SciTech Forum, San Diego, CA, 2022.
[6] R. H. Jansen, J. Scheidler, T. Tallerico, P. Kascak, A. Woodworth, A. D. Smith, R. Dyson, W. Sixel, J. Thompson, E. Stalcup, Y. De Jesus-Arce, D. Avanesian, K. Duffy, P. Passe, and G. Szpak, "High Efficiency Megawatt Motor Risk Reduction Activities," in AIAA/IEEE Electric Aircraft Technologies Symposium (EATS), virtual, 2020.
[7] J. J. Scheidler, T. F. Tallerico, W. A. Miller and W. Torres, "Progress Toward the Critical Design of the Superconducting Rotor for NASA's 1.4 MW High-Efficiency Electric Machine," in AIAA/IEEE Electric Aircraft Technologies Symposium (EATS), Indianapolis, IN, 2019.
[8] J. J. Scheidler, E. J. Stalcup, T. F. Tallerico, W. Torres, K. P. Duffy, and T. T. Mulder, "Static Testing of a Conductively-Cooled, High Temperature Superconducting Rotor for a 1.4 MW Electric Machine in a Thermal Vacuum Chamber," in AIAA/IEEE Electric Aircraft Technologies Symposium (EATS), San Diego, CA, 2023.
[9] G. Szpak, A. Smith, J. Thompson, A. Woodworth and R. Jansen, "High Efficiency Megawatt Motor Thermal Stator Preliminary Design," in AIAA/IEEE Electric Aircraft Technologies Symposium (EATS), virtual, 2020.
[10] E. E. Swanson, H.-H. Tsuei, and P. S. O'Meara, "The Effect of Axial Flow Velocity on Annular Gap Windage Power Loss," In Turbo Expo: Power for Land, Sea, and Air, vol. 50794, p. V02BT42A002, Charlotte, NC, 2017.
[11] D. A. Lowther and P. P. Silvester, "Computer Aided Design in Magnetics," New York: Springer-verlag, 1986.

Acknowledgments
This work was supported by the NASA Advanced Air Transportation Technologies Project - Propulsion & Power Subproject managed by Amy Jankovsky within NASA's Aeronautics Research Mission Directorate. The authors thank their colleague Fred Vankeuls for assisting with test rig operation and sensor troubleshooting.